Constraining Spinning Dust Parameters With the WMAP Five-Year Data

The Astrophysical Journal, 699:1374–1388, 2009 July 10 doi:10.1088/0004-637X/699/2/1374

CONSTRAINING SPINNING DUST PARAMETERS WITH THE *WMAP* FIVE-YEAR DATA

Gregory Dobler[1], Bruce Draine[2], and Douglas P. Finkbeiner[1]
[1] Institute for Theory and Computation, Harvard-Smithsonian Center for Astrophysics, 60 Garden Street, MS-51, Cambridge, MA 02138, USA; gdobler@cfa.harvard.edu
[2] Department of Astrophysical Sciences, Princeton University, Princeton, NJ 08544, USA
Received 2008 November 9; accepted 2009 April 22; published 2009 June 23

ABSTRACT

We characterize spinning dust emission in the warm ionized medium (WIM) by comparing templates of Galactic dust and Hα with the five-year maps from the *Wilkinson Microwave Anisotropy Probe* (*WMAP*). The Hα-correlated microwave emission deviates from the thermal bremsstrahlung (free–free) spectrum expected for ionized gas, exhibiting an additional broad bump peaked at ∼40 GHz which provides ∼20% of the peak intensity. We confirm that the bump is consistent with a modified Draine and Lazarian spinning dust model, though the peak frequency of the emission is somewhat lower than the 50 GHz previously claimed. This frequency shift results from systematic errors in the large-scale modes of the three-year *WMAP* data which have been corrected in the five-year data release. We show that the bump is not the result of errors in the Hα template by analyzing regions of high free–free intensity, where the *WMAP K*-band map may be used as the free–free template. We rule out a pure free–free spectrum for the Hα-correlated emission at high confidence: $\sim 27\sigma$ for the nearly full-sky fit, even after marginalizing over the cosmic microwave background cross-correlation bias. We also extend the previous analysis by searching the parameter space of the Draine and Lazarian model but letting the amplitude float. The best fit for reasonable values of the characteristic electric dipole moment and density requires an amplitude factor of ∼0.3. This suggests that small polycyclic aromatic hydrocarbons in the WIM are depleted by a factor of ∼3.

Key words: diffuse radiation – dust, extinction – ISM: clouds – radiation mechanisms: non-thermal – radio continuum: ISM

1. INTRODUCTION

Following formulation of a physical model (Draine & Lazarian 1998b, hereafter DL98), spinning dust has been invoked to explain the dust-correlated microwave emission seen by the *Wilkinson Microwave Anisotropy Probe* (*WMAP*) from 23 to 41 GHz (de Oliveira-Costa et al. 2004; Finkbeiner 2004; Finkbeiner et al. 2004; Boughn & Pober 2007; Dobler & Finkbeiner 2008b). Given the *WMAP* data at 94 GHz, the dust-correlated emission at 23–41 GHz was anomalously high to be explained by a purely thermal emission mechanism.

Bennett et al. (2003) attempted to obviate the inconsistency by suggesting that the first-year data from *WMAP* did not require a spinning dust component to construct an internally consistent foregrounds model, so long as the dust-correlated emission was actually dust-correlated synchrotron at low frequencies. However, when the three-year *WMAP* data (23–94 GHz) were combined with lower frequency data from Green Bank (8, 14 GHz; Finkbeiner et al. 2004), Tenerife (10, 15 GHz; de Oliveira-Costa et al. 2004), and other telescopes (19 GHz; Boughn & Pober 2007), it became clear that the dust-correlated emission at ∼20 GHz did not behave spectrally like synchrotron emission, and was instead consistent with a spinning dust spectrum.

The principal source of ambiguity in interpreting the low-frequency *WMAP* data as evidence for spinning dust was that the spectrum of the dust-correlated emission falls from 23 to 41 GHz. The implication is that either the peak in the spectrum is near or below the lowest *WMAP* band or that the emission is synchrotron, and it is only with data at lower frequency that the spinning dust spectrum is recovered. In the DL98 spinning dust models, however, the peak frequency of the spinning dust emission varies depending on model parameters (e.g., the grain size, geometry, ambient density, etc.), and at higher temperatures is expected to be ∼40 GHz. This regime is termed the "warm ionized medium" (WIM, $T \sim 8000$ K) in DL98 compared to the "cold neutral medium" (CNM, $T \sim 100$ K) emission that peaks at ∼20–30 GHz and is thought to be the source of the dust-correlated emission at low frequencies in *WMAP*.

Dobler & Finkbeiner (2008b, hereafter DF08b) showed that the ambiguity is eliminated and that the turnover in the spinning dust spectrum is recoverable *within* the *WMAP* frequency range using Hα-correlated emission as a tracer of WIM spinning dust emission. Typically, Hα is used as a tracer of free–free (thermal bremsstrahlung) emission from $\sim 10^4$ K gas in regions where extinction from dust is minimal. However, because a map of Hα represents an emission measure (EM; density squared integrated along the line of sight) and because spinning dust emission is generated via dust grains that are spun up by collisions with ions (which should also be roughly proportional to density squared integrated along the line of sight), the Hα emission should also spatially trace WIM spinning dust emission.[3] In the analysis of DF08b, the peak frequency of the emission was found to be ∼50 GHz, which was slightly higher than the ∼40 GHz predicted by DL98.

In this paper, we show that the evidence for spinning dust in the Hα-correlated emission has strengthened with the release of the five-year data, due to both decreased noise as well as corrections made to large-scale fluctuations that were present in the three-year data.

2. TEMPLATE FITS

Microwave emission mechanisms in the *WMAP* frequency range can be separated into four broad categories: free–free,

[3] Finkbeiner et al. (2004) showed that there is evidence for a deviation from a pure free–free spectrum even in the H II region W40 which is highly free–free dominated, see their Figure 8.

thermal dust, spinning dust, and synchrotron emission.[4] Free–free emission is generated by electron–ion collisions in ionized gas; thermal dust refers to electric dipole emission from thermal fluctuations (e.g., lattice vibrations) in the electric charge distribution in the grain; and spinning dust is electric dipole radiation from the smallest dust grains which are rotationally excited by a variety of collisional mechanisms. Synchrotron emission consists of a soft component ($T \propto \nu^{-\beta_S}$ with $\beta_S \approx 3$) originating from supernova-shock-accelerated electrons which spiral around the Galactic magnetic field and a hard component ($\beta \approx 2.5$) centered on the Galactic center and extending roughly 20°. This hard component has been termed the "haze" and its origin remains uncertain (Finkbeiner 2004; Dobler & Finkbeiner 2008a).

Each of these emission mechanisms is approximately traced by maps of the sky at other frequencies, described below. This external information about the spatial structure of the foregrounds makes possible a multi-linear fit of the spectrum of each foreground. This multi-linear regression may be performed over the whole sky, or in selected regions to study the spectral variation of each component. We now briefly describe the templates used, and the fitting method (see Dobler & Finkbeiner 2008a for more details).

2.1 The Templates

For fitting purposes, we distinguish between the soft synchrotron component originating from supernova-shock-accelerated electrons, and a harder synchrotron component in the inner Galaxy, possibly with a different physical origin. Soft synchrotron emission is well traced by the Haslam et al. (1982) 408 MHz map. Though the spectral index of this emission is expected to vary slightly from place to place in the sky, La Porta et al. (2008) showed that from 408 to 1420 MHz, $T \propto \nu^{-\beta_S}$ with $\beta_S \approx 3$. A similar spectral index was derived by Page et al. (2007) using polarization in the *WMAP* data.

The *WMAP* data, even in the first year, contained evidence of a harder synchrotron component in the inner Galaxy, which has become known as the "haze" because of its relatively featureless morphology (Finkbeiner 2004). Dobler & Finkbeiner (2008a, hereafter DF08a) interpret the haze as a separate physical component in the template fit described in DF08a and below, and the spectrum of this emission was found to be $T \propto \nu^{-\beta_H}$ with $\beta_H \approx 2.5$. The template we use for this component is $T \propto 1/r_{\rm gal}$, where $r_{\rm gal}$ is the distance from the Galactic center in degrees. Though systematics related to contamination of any cosmic microwave background (CMB) template by residual foregrounds leads to uncertainty in the derived soft and hard synchrotron spectra, we note that neither the presence nor the spectrum of the haze has any significant effect on the conclusions in this paper. For a detailed study of microwave synchrotron in the Galaxy, see G. Dobler & D. P. Finkbeiner (2009, in preparation).

Our thermal dust template is the Finkbeiner et al. (1999, hereafter FDS99) two-component model of thermal dust, evaluated at 94 GHz. The FDS99 map uses column densities and temperatures from *IRAS*/ISSA (Wheelock et al. 1994) and *COBE*/DIRBE (*COBE* DIRBE Exp. Supp. 1995) given by Schlegel et al. (1998; SFD), constrained to fit *COBE*/FIRAS data in the microwave and submillimeter (*COBE* FIRAS Exp. Supp. 1997). The preferred FDS99 model (model 8) gives $I_\nu \propto \nu^{1.7} B_\nu(T_{\rm dust})$. Converting this to antenna temperature, $T \propto \nu^{\beta_D}$ with $\beta_D \approx 1.55$ in the *WMAP* bands for typical $T_{\rm dust}$ values. We use the same template for the diffuse, CNM spinning dust which has a peak frequency ∼20 GHz.

For a free–free and WIM spinning dust template, we use the Hα map assembled by Finkbeiner (2003) using data from three surveys: VTSS (Dennison et al. 1998), SHASSA (Gaustad et al. 2001), and WHAM (Haffner et al. 2003). The template is corrected for dust extinction assuming the dust and ionized gas are uniformly mixed along the line of sight. This approximation fails in regions of very high dust column density, so we mask out regions in our fit where the SFD extinction at Hα is $A(\mathrm{H}\alpha) \equiv 2.65E(B-V) > 1$ mag. Additionally, we mask out all point sources listed in the WMAP5 point-source list as well as the LMC, SMC, M31, Orion-Barnard's Loop, NGC 5090, and the H II region around ζ Oph. This mask covers 22.2% of the sky and is shown in Figure 2 below. Roughly 1/4 of the masked pixels are point sources.

2.2. CMB Estimators

Finally, we also need an estimator for the CMB since it contributes a large variance at *WMAP* frequencies (and in fact constitutes the *biggest* source of noise when deriving foreground properties). We use the six CMB estimators described in DF08a and summarize their features in Table 1. As noted in DF08a (see also Hinshaw et al. 2007), every CMB estimator is contaminated to varying degrees by foregrounds which leads to a systematic bias in the inferred foreground spectra. In the case of "internal linear combination" (ILC) type estimators, in which the *WMAP* maps in each band b are weighted and summed with weight coefficients ζ_b that are chosen to approximately cancel the foregrounds while preserving unity response to the CMB, the bias is proportional to the chance spatial correlation of the true foregrounds (as opposed to the templates) with the CMB (see DF08a).

The spectral cross-correlation coefficients given in, e.g., Figure 6 depend on the CMB estimator used, but because we fit out a CMB spectrum in the interpretation of the correlation spectra (see Section 5), *the final results for the Hα-correlated spinning dust do not depend on our choice of CMB estimator*.

2.3. Template Fit Procedure

To infer the spectra of the individual foreground components, we use the multi-linear regression template fit described in DF08a. We construct the template matrix P, whose columns consist of the templates described above, and derive the spectrum of the template-correlated emission, a_b^i, where $\mathbf{a}^i$ denotes the spectrum of foreground i and $\mathbf{a}_b$ is the vector of correlation coefficients for band b. For each band, we solve the matrix equation,

$$P\mathbf{a}_b = \mathbf{w}_b, \tag{1}$$

for $\mathbf{a}_b$, where $\mathbf{w}_b$ is the *WMAP* map for band b. To determine the best fit $\mathbf{a}_b$ in Equation (1), we evaluate the "pseudoinverse" P^+ (see DF08a) and note that $\mathbf{a}_b = P^+\mathbf{w}_b$ minimizes the quantity $\Delta^2 \equiv \sum_p |P\mathbf{a}_b - \mathbf{w}_b|^2$ where the sum is over unmasked pixels.

[4] Draine & Lazarian (1999) point out that if interstellar dust contains an appreciable fraction of ferrimagnetic or ferromagnetic materials, thermal fluctuations in the magnetization would generate appreciable amounts of magnetic dipole emission at frequencies $\nu < 100$ GHz, which would be a fifth type of CMB foreground. However, Casassus et al. (2008) find that this type of emission is inconsistent with the morphology of cm emission from the ρ Oph cloud, implying that magnetic materials are not abundant in interstellar dust. Thus, we do not consider it further in this paper; we will use the term "thermal" emission to refer specifically to emission from thermal fluctuations in the electric dipole moments of grains.

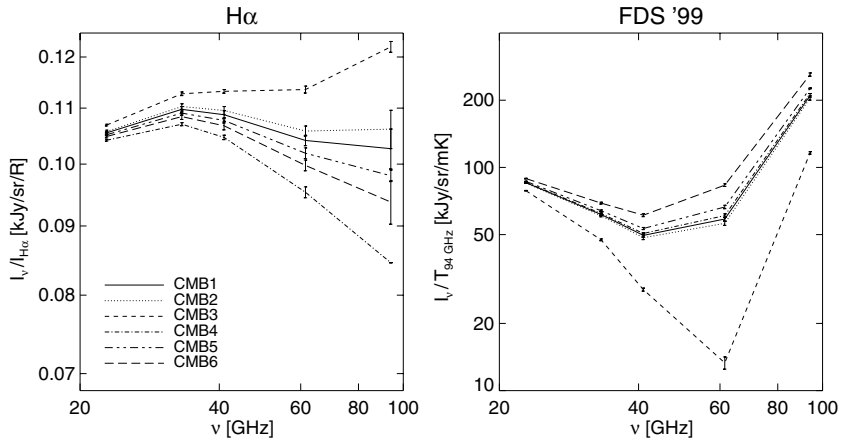

Figure 1. Cross-correlation spectra for the Hα (left) and FDS99 dust (right) templates using various estimators of the CMB anisotropy (see Section 2.2). Although the formal error in the fit is small, in both cases the unknown degree of CMB contamination introduces a highly covariant uncertainty. In each case, the spectra are the same up to addition of a CMB spectrum of unknown amplitude.

Table 1
The Different Types of CMB Estimators Used in the Fits

CMB Type	Description	ILC coefficients				
		K	Ka	*Q*	*V*	*W*
1	Published *WMAP* five-year ILC[a]			N/A		
2	ILC using *WMAP* five-year Kp2 coefficients	0.134	−0.646	−0.377	2.294	−0.405
3	Minimum variance ILC over unmasked, fit pixels	0.048	−0.603	0.342	0.530	0.683
4	*WMAP W* band minus (thermal dust + free–free model)			N/A		
5	Minimum variance ILC with thermal dust model presubtracted	0.182	−0.638	0.044	0.325	1.086
6	TOH five-year map[b]			N/A		

Notes. Because of contamination of these estimators by foregrounds, the inferred foreground spectra vary depending on the estimator used. Our preferred estimator is CMB5, which consists of an ILC with a minimum variance (over unmasked pixels) weighting of the thermal dust model presubtracted *WMAP* data. One of the attractive features of this map is that it has well understood noise properties.

[a] Available at http://lambda.gsfc.nasa.gov/.

[b] M. Tegmark et al. (2008, private communication).

Dividing P and $\mathbf{w}_b$ by σ_b (the mean noise in each band,[5] as in Bennett et al. 2003; Hinshaw et al. 2007), this solution for $\mathbf{a}_b$ minimizes

$$\left\| \frac{P}{\sigma}\,\mathbf{a}_b - \frac{\mathbf{w}_b}{\sigma_b} \right\|^2 = \frac{\|P\mathbf{a}_b - \mathbf{w}_b\|^2}{\sigma_b^2} \equiv \chi_b^2. \qquad (2)$$

The total $\chi^2 = \sum_b \chi_b^2$ for the fit is given by the sum over the five *WMAP* bands. We also define the residual maps $\mathbf{r}_b \equiv \mathbf{w}_b - P\mathbf{a}_b$.

With our template fits, the spectrum of each foreground emission component $\mathbf{a}^i$ is left completely unconstrained, though it is assumed to be constant across the sky. To appropriately account for the CMB, we also force $\mathbf{a}^{\rm CMB} = 1$ in units of thermodynamic temperature.

3. FOREGROUND CROSS-CORRELATION SPECTRA

Our foreground spectrum fits are characterized by the cross-correlation coefficient $\mathbf{a}$ as well as the formal error in the fit in each band. These errors take into account both the noise in each *WMAP* band and morphological correlations between the different templates. By our definition of $\mathbf{a}$ above, the derived (cross-correlation) spectra are in I_ν units of kJy sr^{-1} per template unit—Rayleighs for Hα-correlated emission and mK for FDS99-correlated emission. Both the data and templates are mean subtracted over unmasked pixels to remove sensitivity to zero-point levels in the maps.

3.1. Hα and Dust-Correlated Emission

Figure 1 shows our derived cross-correlation spectra for the Hα- and FDS99-correlated microwave emission from 23 to 94 GHz for our six CMB estimators. The dust-correlated spectrum exhibits the familiar thermal tail from 94 to 61 GHz and then the rise from ∼50 to 23 GHz from anomalous emission. While the statistical error bars[6] on the spectra are very small due to both the high sensitivity of *WMAP* as well as the large sky coverage (∼150,000 pixels for HEALPix $N_{\rm side} = 128$), the systematic effects from the contamination of the CMB estimators by foregrounds are significant.

As identified in DF08a and DF08b, the spectrum of Hα-correlated emission does *not* follow the free–free power law as expected. Instead, there is a bump in the spectrum with a peak frequency $\nu_{\rm p} \approx 40$ GHz. This bump is present for all CMB estimators. We note that it cannot be generated by a contamination of the CMB estimator by foregrounds (since this bias has the spectrum of the CMB) and DF08b argued that this bump is most easily explained by a WIM spinning dust component that is traced by the Hα map. We address both of these considerations in detail below.

[5] The *WMAP* scan strategy visits some pixels, e.g., the ecliptic poles, far more than average. Because we are in the systematics-dominated limit, we use the average noise in each band to avoid overweighting certain parts of the sky.

[6] The error bars include the absolute calibration error for *WMAP* which is ∼0.5% (G. Hinshaw 2008, private communication).

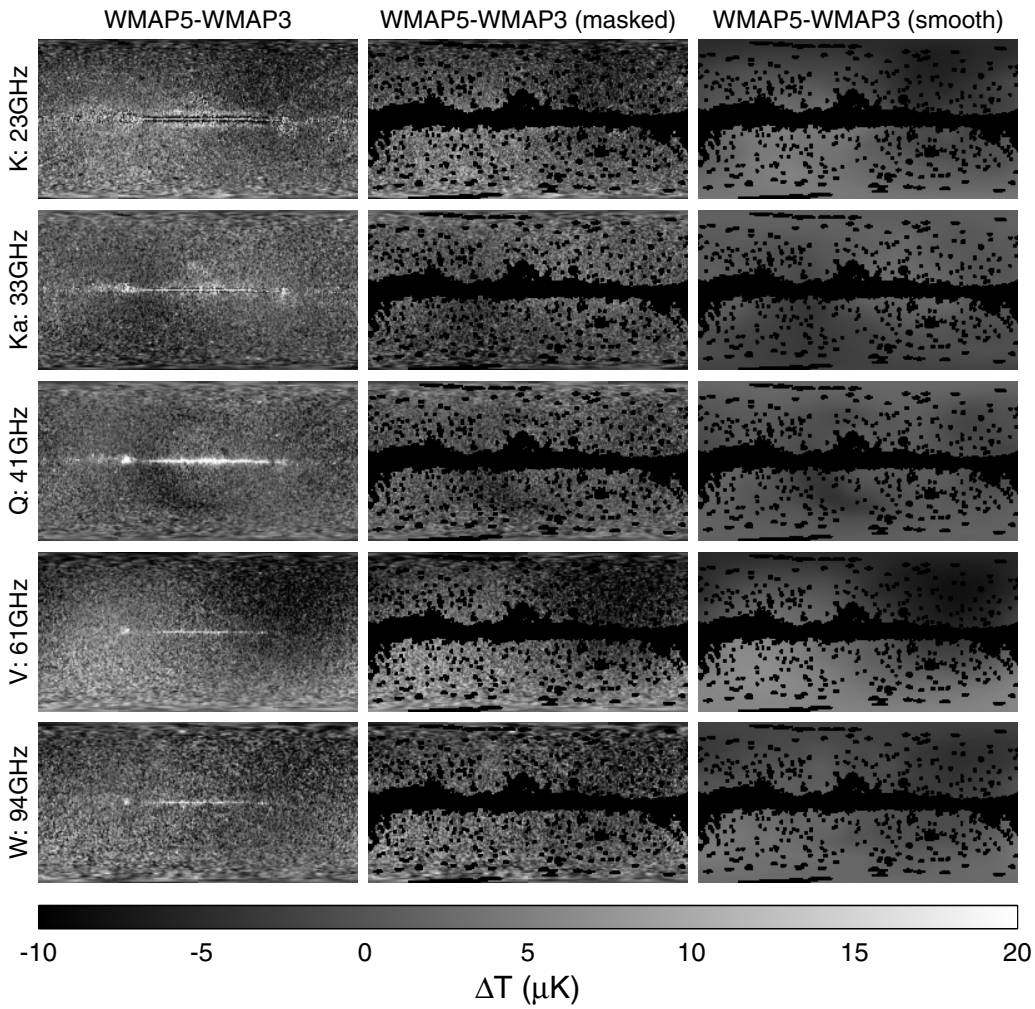

Figure 2. The difference between the *WMAP* five-year and three-year data in the five bands. Left: WMAP5−WMAP3. Updated beams and gains lead to differences in the plane; however, large-scale gradients (and in some cases dipoles) are seen in each band. Center: WMAP5−WMAP3 masked with the pixels that are used in the multi-linear regression fit (see Section 2). Right: WMAP5−WMAP3 smoothed to 30° FWHM and masked. Here, the large-scale fluctuations are clearly evident. In particular, the peaks range from ~ -8 μK to $\sim$15 μK. All maps were mean subtracted over unmasked pixels prior to subtraction and smoothing.

3.2. Changes From Three-Year to Five-Year Data

There are two notable differences when comparing our results using the three-year versus five-year *WMAP* data. First, the inferred peak frequency $\nu_{\rm p} \approx 40$ GHz is significantly lower than the 50 GHz seen in the three-year *WMAP* data (see DF08b). This shift in peak frequency is primarily due to spurious large-scale power that was present in the three-year data but has been corrected in the five-year data release. Figure 2 shows that the amplitude of these fluctuations can be quite large. In particular, the *V*-band dipole is clearly apparent and has peak values from ~ -7 μK to $\sim$10 μK.

As described above, we have mean subtracted the maps over unmasked pixels to perform the template fits, and so our results are not sensitive to zero-point offsets. However, if there is spurious low ℓ power, as in the three-year data, our fit results will be affected. Hinshaw et al. (2009) point out that these large-scale fluctuations in the three-year data were due to imperfect characterization of the instrument gain. While the amplitudes of the fluctuations are not large enough to have a significant impact on CMB analyses, Hα-correlated emission mechanisms (free–free and WIM spinning dust) are sufficiently subdominant at *WMAP* frequencies that $\sim$10 μK offsets become important. Because the 61 GHz band (*V* band) was the most affected, and because the WIM spinning dust peak frequency is in the range 30–50 GHz, it is not surprising that our best-fit peak frequency has shifted. Had the spurious low-ℓ power been morphologically similar in all bands, the peak frequency would have been similar between the three- and five-year data. The problem was exacerbated by the CMB estimators, which necessarily contained some complicated combination of these fluctuations.

The second difference between the three- and five-year analyses is that, for a given CMB estimator, the ILC coefficients (defined in Equation (4) below) have changed. Although this does not affect our interpretation of the fit results (see Section 5), the spectrum of Hα-correlated emission has also changed by more than the formal fit uncertainties. Since this is due primarily to changes in the coefficients used when constructing a CMB estimator, the extent of the contamination of these estimators by foregrounds has changed from year three to year five. For example, in the case of a simple ILC which minimizes the variance over unmasked pixels (CMB3) with respect to the ILC coefficients ζ_b,

$$\frac{\partial \langle T_{\rm ILC}^2 \rangle}{\partial \zeta_b'}\Big|_{\zeta_b'=\zeta_b} = 0, \quad (3)$$

Table 2
Spinning Dust Parameters for the "Warm Ionized Medium" (WIM) and "Cold Neutral Medium" (CNM) Environments

Environment	$n_{\rm H}$ (cm^{-3})	μ_0 (D)	$T_{\rm gas}$ (K)	$T_{\rm dust}$ (K)	$x_{\rm H}$	$x_{\rm M}$	χ	y
WIM	0.01–0.6	0.5–12	3000	20	0.99	0.001	1.0	0.0
CNM	5.0–40.0	0.5–12	100	20	0.0012	0.0003	1.0	0.0

Note. For a detailed definition of the parameters shown here, see DL98.

where

$$T_{\rm ILC} = \sum_b \zeta_b \mathbf{w}_b \tag{4}$$

is the ILC map in thermodynamic mK and the ILC coefficients ζ_b are constrained to sum to unity to preserve response to the CMB. These coefficients are sensitive not only to the large-scale fluctuations mentioned above, but also to the *noise* in the measurements themselves since $\mathbf{w_b} = \mathbf{c} + \mathbf{f}_b + \mathbf{n}_b$, where $\mathbf{c}$, $\mathbf{f}_b$, and $\mathbf{n}_b$ are the CMB, total foregrounds in each band, and noise in each band, respectively. Thus, the signal variance in the noise also contributes to the determination of ζ_b. This is illustrated by the limit of large measurement noise, in which case the minimum variance linear combination would have $\zeta_b = 1/\sigma_b^2$.

3.3. Hα as a Tracer of Spinning Dust

For the three-year *WMAP* data, DF08b presented an argument for why the Hα map should trace spinning dust emission at *WMAP* frequencies. Briefly, the Hα intensity is proportional to the EM, $\int n_e^2 d\ell \equiv$ EM, where n_e is the electron density and the integral is along the line of sight. We will show below that evaluating the DL98 spectrum with parameters appropriate for the WIM, the total emission is indeed roughly proportional to n_e^2. That is, including other (de-)excitation mechanisms such as plasma drag, far-infrared emission from the grains, etc., the behavior of the total emission with density implies that the Hα EM map should trace a component of the spinning dust emission in the Galaxy.

4. SPINNING DUST MODEL

In this section, we summarize the spinning dust model used in our analysis of the five-year Hα- and dust-correlated spectra below. The model for excitation mechanisms and dipole moment distributions is described in detail in DL98. We find that the most relevant parameters are the density, $n_{\rm H}$, and the typical electric dipole moment of 1 nm grains, μ_0.

We use the updated grain size distribution given in Draine & Li (2007). Our grain size distribution is a double log-normal distribution characterized by a mean and width for the small and large grain populations—$\langle a \rangle = 4$ and 20 Å and $\sigma_a = 0.4$ and 0.55, respectively (Draine & Li 2007). This size distribution has a lower cutoff of $a_{\rm min} = 3.55$ Å which corresponds to $N_{\rm atoms} = 20$ carbon atoms. The dipole moment distribution for the grains consists of three delta functions so that 50% of the grains have $\mu = \mu_0(a/1\ {\rm nm})^{3/2}$, 25% have μ half as large, and 25% have μ twice as large.

The spinning dust emission in the DL98 model comes from polycyclic aromatic hydrocarbons (PAHs) of very small size, $N_{\rm atom} \sim 100$ or less. Small asymmetries in the grain geometry result in nonzero dipole moments that are taken to scale with the number of atoms as $\mu \propto \sqrt{N_{\rm atom}}$. As these grains are spun up by various excitations processes (see DL98), they emit electric dipole radiation with total power $P \propto \mu^2\omega^4$, where $\omega/2\pi$ is the rotation frequency and is tens of GHz.[7]

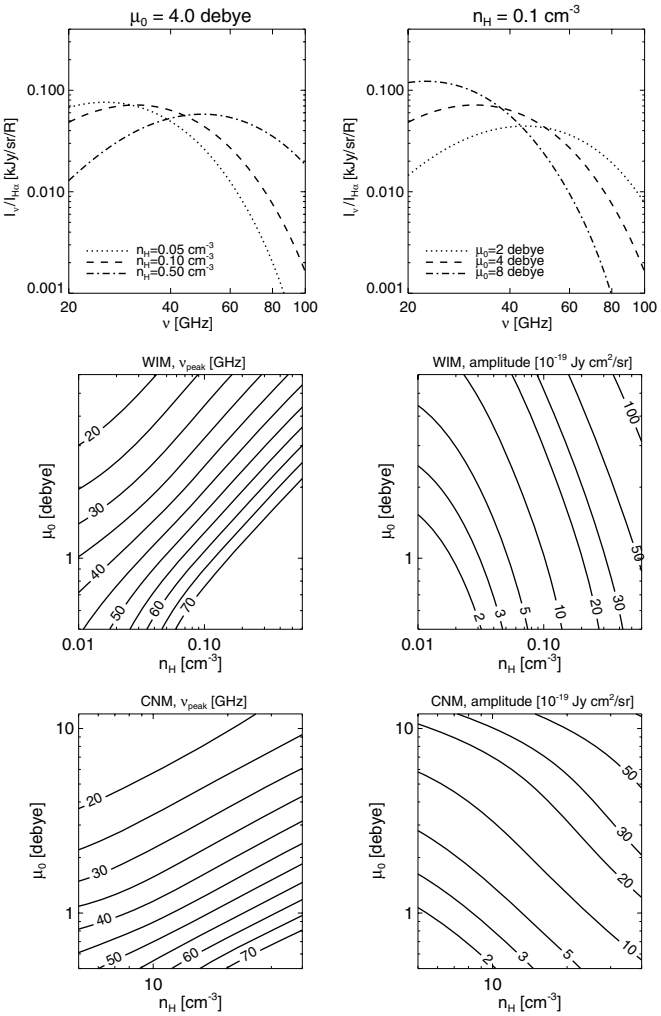

Figure 3. Upper left: spinning dust emission per Hα intensity for WIM parameters, keeping μ_0 constant and varying $n_{\rm H}$. Increasing $n_{\rm H}$ increases the peak frequency but changes the total power per Hα little. Upper right: same, but for constant $n_{\rm H}$ and varying μ_0. Decreasing μ_0 also increases the peak frequency but decreases the total power per Hα. Note that in this part of $(n_{\rm H}, \mu_0)$ parameter space, the shape of the spectrum is nearly unchanged, but shifts in frequency and amplitude. Middle panels: contours of the peak frequency (left) and peak amplitude (right) in the $(n_{\rm H}, \mu_0)$ plane. Lower panels: same, but for CNM parameters. See the discussion in Section 4 for details.

The parameters which characterize the environment and grain properties, with values appropriate for the WIM and CNM, are summarized in Table 2. The top two panels of Figure 3 show example spinning dust spectra for WIM parameters while

[7] An improved treatment of the spinning dust problem by Ali-Haïmoud et al. (2009) has made a few refinements of the DL98 model but those modifications do not significantly affect the results of this paper.

holding the density $n_{\rm H}$ fixed while varying the characteristic dipole moment μ_0 and vice versa. These spectra are in units of $I_\nu/I_{\rm H\alpha}$, or total intensity per intensity at Hα with $T_{\rm gas} = 3000$ K (our justification for using this gas temperature, which is lower than the commonly used 8000 K, is given in Section 5.1). For fixed μ_0, as $n_{\rm H}$ is increased the spectrum shifts up in frequency with very little change in overall power per Hα. Since $I_{\rm H\alpha} \propto n_{\rm H}^2$ in fully ionized environments, the total spinning dust intensity goes roughly like $n_{\rm H}^2$. This point will be explored in more detail shortly, but it illustrates that an EM map like the Hα map should trace WIM spinning dust emission.

For fixed $n_{\rm H}$, as μ_0 is increased Figure 3 shows that the spectrum increases in amplitude and decreases in peak frequency. This can be understood in terms of the radiated power per grain which goes as μ^2: grains with larger dipole moments radiate away power faster and are thus harder to spin up leading to a lower peak frequency, but they also emit more total power leading to an increased amplitude.

The lower four panels of Figure 3 are contour plots showing the effects of varying $n_{\rm H}$ and μ_0 on the amplitude and peak frequency of the spinning dust spectrum. Contours are shown for both the WIM and CNM conditions. The contours of peak frequency show that if the amount of dust per H is assumed unknown (i.e., the amplitude is allowed to vary), then there is a strong degeneracy in the peak frequency between $n_{\rm H}$ and μ_0. The implication of this strong degeneracy is that a measurement of the spinning dust spectrum with sparse frequency sampling that only gives information about the peak frequency (as is the case with the *WMAP* data below, see Figure 8) cannot uniquely constrain these two parameters. On the other hand, if the grain abundance is assumed known, then the degeneracy is broken and the parameters are more tightly constrained.

Figure 4 shows how the spectrum of spinning dust emission changes with the dipole moment distribution of the grains. Three different distributions are shown: our benchmark distribution described above, as well as narrower and broader distributions. As the dipole moment distribution is broadened, the resultant spinning dust spectrum is correspondingly broader, and the peak frequency shifts to lower values. Similarly, a very narrow distribution results in a narrower spectrum with higher peak frequency. Since little is known about the specific distribution of grain dipole moments, we concentrate on our benchmark model throughout the rest of this paper and do not explore deviations from it further.

Figure 5 shows the behavior with $n_{\rm H}$ of the emissivity per EM for both the total emission, $\int j_\nu d\nu$, as well as νj_ν evaluated at the five *WMAP* frequencies. The parameters of the WIM and CNM environments are also given in Table 2 while those for the reflection nebula (RN) and photodissociation region (PDR) are shown on the plot. In the limit of low $n_{\rm H}$, all four environments exhibit roughly $j_\nu \propto n_{\rm H}$ behavior. In this limit, the dominant excitation and de-excitation mechanism are absorption and emission of infrared photons and thus the total emission scales linearly with density. This is in contrast to the argument presented in DF08b who argued that in the lowest density regions, the grains are in the episodic limit and so the total emission should scale as $n_{\rm H}^2$. That argument neglected the importance of photon interactions.

While the linear $n_{\rm H}$ scaling persists through all densities shown here for the RN and PDR regions, the WIM and CNM both flatten to $j_\nu \propto n_{\rm H}^2$ behavior at $n_{\rm H} \sim 0.01$ and 5 cm^{-3}, respectively. In this regime, the dominant spin up mechanism is collisions with ions and the $n_{\rm H}^2$ scaling persists for 4 orders of magnitude in $n_{\rm H}$ for the WIM ($\sim 10^{-2}$–10^2 cm^{-3}). As the density increases further in the CNM, the spectrum turns over and again goes roughly like $j_\nu \propto n_{\rm H}$. At these high densities, both spin up and damping are dominated by thermal processes (collisions with ions and atoms). However, it is interesting to note that over the density ranges shown in Table 2, both the WIM and CNM models scale as $n_{\rm H}^2$. Since the WIM has a large EM, this indicates that a map that scales with EM like *the Hα map should trace WIM spinning dust emission*.

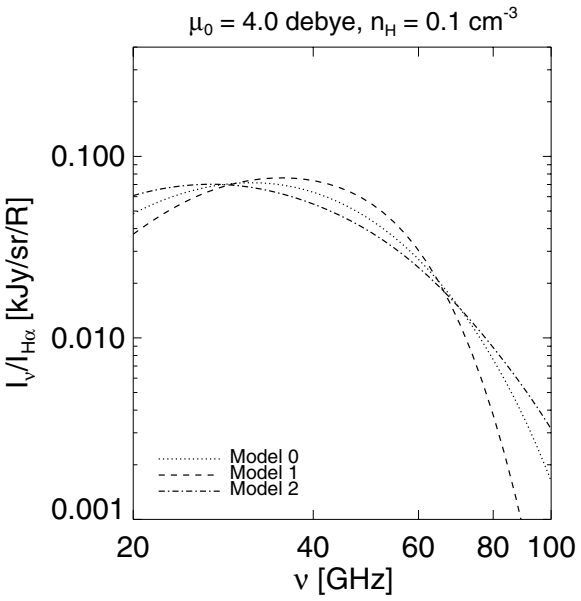

Figure 4. Spinning dust emission per Hα intensity for WIM parameters and for three different dipole moment distributions. Model 0 (dotted): the benchmark distribution used throughout this paper, where 50% of the grains have $\mu = \mu_0(a/1\ {\rm nm})^{3/2}$, 25% have μ half as large, and 25% have μ twice as large. Model 1 (dashed): a narrower distribution with a single delta function at $\mu = \mu_0(a/1\ {\rm nm})^{3/2}$. Model 2 (dot dashed): a broader distribution with five delta functions such that 40% of the grains have $\mu = \mu_0(a/1\ {\rm nm})^{3/2}$, 10% have μ a quarter as large, 10% have μ four times as large, 20% have μ half as large, and 20% have μ twice as large. Broadening (narrowing) the dipole moment distribution results in a correspondingly broader (narrower) spinning dust spectrum. Broadening the distribution also slightly lowers the peak frequency.

5. THREE-COMPONENT FOREGROUND SPECTRA

Given that the Hα map should trace both the free–free and a spinning dust emission component, and given the fact that our foreground spectra are necessarily contaminated by a component with the spectrum of the CMB (flat in thermodynamic ΔT) from the CMB cross-correlation bias described in DF08a and Section 2, we interpret the Hα-correlated emission in Figure 1 as a three-component spectrum. As in DF08b, we fit a free–free plus CMB plus DL98 WIM spinning dust model,

$$I_\nu^{\rm mod} = F_0 \left(\frac{\nu}{23\ {\rm GHz}}\right)^{-0.15} + C_0 \left(\frac{\nu}{23\ {\rm GHz}}\right)^2 \frac{1}{{\rm plc}(\nu)} + D_0 \times ({\rm DL98\ WIM}), \quad (5)$$

to the measured cross-correlation spectrum I_ν. Here, plc is the "Planck correction" factor which converts thermodynamic ΔT to antenna temperature at frequency ν (*COBE* FIRAS Exp. Supp. 1997). We choose the parameters $n_{\rm H}$ and μ_0, generate a spinning dust spectrum, and minimize $\chi^2 \equiv \sum_i (I_\nu - I_\nu^{\rm mod})^2/\sigma_i^2$, where σ_i are the errors in the fit in each band i, over the parameters F_0,

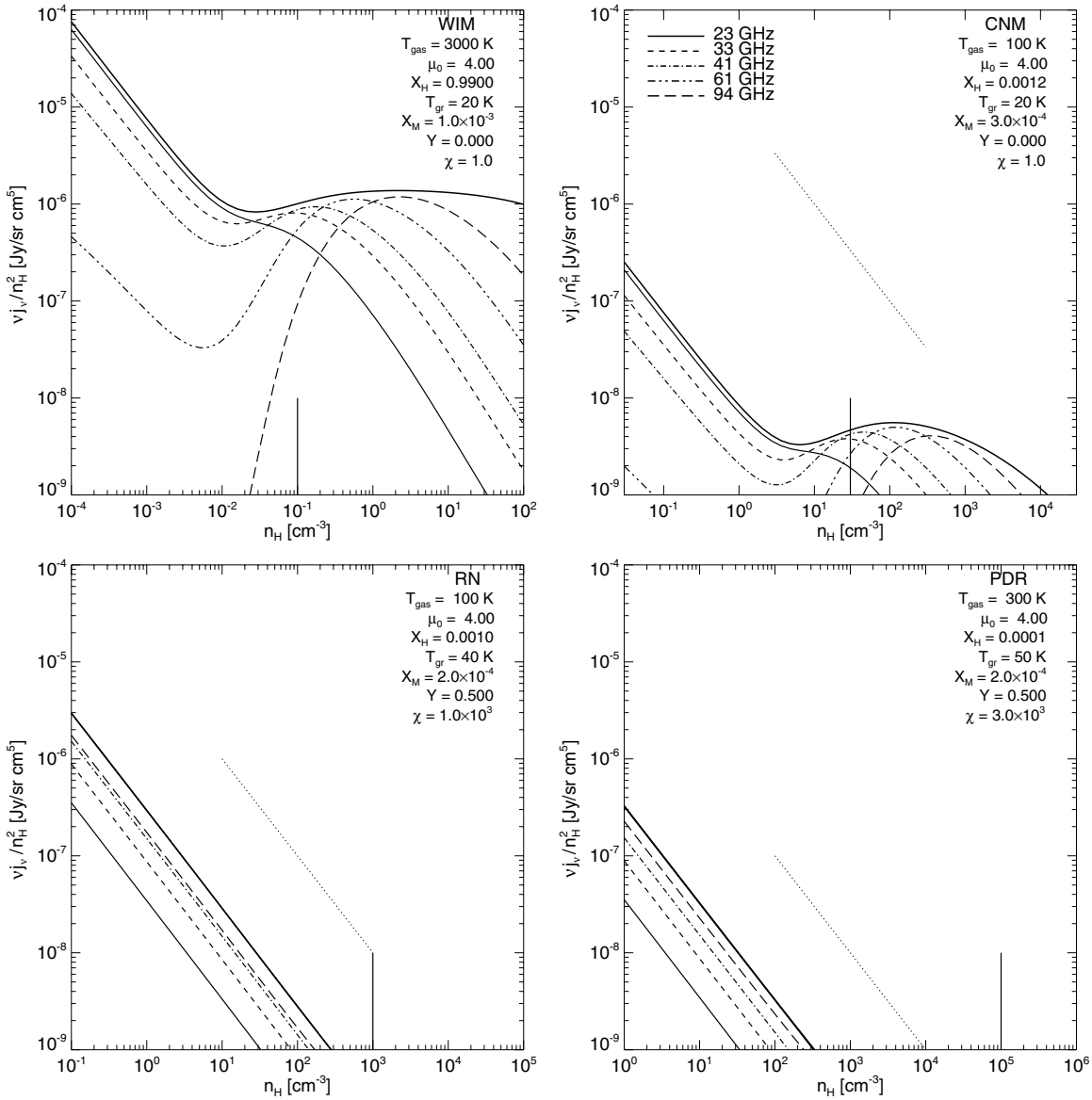

Figure 5. Spinning dust emission per $n_{\rm H}^2$ for the WIM (upper left), CNM (upper right), RN (lower left), and PDR (lower right). Each panel contains $\nu j_\nu/n_{\rm H}^2$ for the five *WMAP* bands: 23 GHz (solid), 33 GHz (dashed), 41 GHz (dash dot), 61 GHz (dash triple-dot), and 94 GHz (long dash). The upper solid line is the integrated emissivity, $\int j_\nu d\nu/n_{\rm H}^2$. Some panels include a line slope of -1 (dotted), corresponding to $j_\nu/n_{\rm H}$ constant with $n_{\rm H}$. This limit is generally approached when photons dominate, either because of low density or intense radiation field. The solid vertical line marks the value chosen by DL98 for each environment.

C_0, and D_0. We allow D_0 to float in the fit because of uncertainty about the PAH size distribution and abundance in the WIM. We concentrate on CMB5, but our results are minimally changed for the other CMB estimators: it is only the value of C_0 which is significantly affected.

5.1. Hα-Correlated Emission

Figure 6 shows the results of our three-component fit for the Hα-correlated emission. From the figure, it is clear that a spinning dust spectrum with $n_{\rm H}$ and μ_0 set to 0.15 cm^{-3} and 3.5 D, respectively (and with the WIM parameters in Table 2) fits the data remarkably well. This value for μ_0 is comparable to the earlier estimates in DL98. This spectrum has a peak frequency of $\nu_{\rm p} = 37.2$ GHz and D_0 fit coefficient of 0.33. It is interesting to note that the value of D_0 is less than unity. This may indicate either that PAHs are depleted in the diffuse WIM by a factor of ∼3 or that the grain size distribution differs from that in the CNM from which the values of the log-normal mean and width of our grain size distribution were derived (Draine & Li 2007).

From the amplitude of the F_0 fit coefficient, we can derive a gas temperature in the WIM which we find to be $T_{\rm gas} \approx 3000$ K. This is the origin of the choice of $T_{\rm gas}$ in the WIM spinning dust model. This value for $T_{\rm gas}$ is much lower than the temperature inferred from emission line ratios (e.g., see Madsen et al. 2006). We stress that this low gas temperature is *not* the result of assigning some of the intensity to a spinning dust component. Ignoring the bump and merely fitting the data with a free–free only spectrum still gives a gas temperature below 5000 K. Using a technique similar to ours, Davies et al. (2006) also report anomalously low gas temperatures based on the free–free to Hα ratio in the *WMAP* one-year data and DF08b found similar temperatures in the three-year data. The origin of this discrepancy is unclear, though it may result from temperature variations in the WIM along the line of sight as discussed

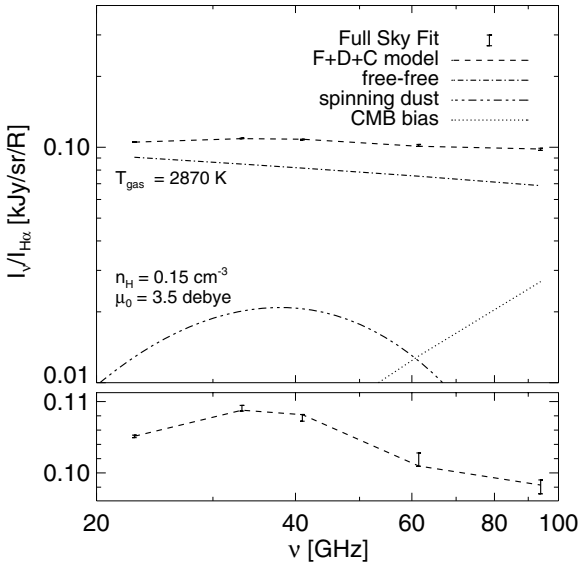

Figure 6. Upper: the Hα-correlated spectrum from 23 to 94 GHz (points) using CMB5 and the three-component fit to the data (dashed line). The three components, free–free, spinning dust, and CMB, are shown separately. The amplitude of the free–free component yields $T_{gas} \approx 3000$ K, while the amplitude of the spinning dust component is less than unity indicating that either PAHs are depleted in the WIM or the grain size distribution is altered. Lower: a zoom in of the spectrum showing that, although the bump is subtle, the statistical significance is very high.

in Heiles (2001).[8] We will explore implications of a two-component temperature model in future work. Lastly, we find that the total intensity in Hα-correlated spinning dust emission is roughly 25% of that in free–free emission at 41 GHz.

The upper panel in Figure 6 shows that the bump in the spectrum is indeed subtle, but the zoom in beneath reveals that it is highly statistically significant. Since we minimize χ^2 over three amplitudes (F_0, D_0, and C_0), set the values of n_H and μ_0 by hand, and fit to five data points, the number of degrees of freedom is formally zero, though with a strong prior on n_H and μ_0. However, Figures 7 and 8 show that the χ^2 rises quickly as we deviate from these parameters. In the left panel of Figure 7, $\Delta\chi^2$ contours are shown in the (D_0, C_0) plane and it is clear that the null hypothesis that the Hα-correlated emission is simply a linear combination of free–free plus a CMB bias (i.e., $D_0 = 0$), is ruled out at very high confidence. In fact, we find that the $D_0 = 0$ case is ruled out at $\sim 27\sigma$. The right panel shows χ^2 contours in the (D_0, ν_p) plane as ν_p is varied by hand. This parameter is less well constrained but is broadly consistent with $\nu_p \sim 35$–40 GHz.

Figure 8 shows χ^2 and D_0 contours in the (n_H, μ_0) plane for the full-sky fit. The χ^2 contours show that there is a long narrow valley in the χ^2 surface reflecting the degeneracy in peak frequency shifts resulting from varying n_H and μ_0 (see Figure 3). Since varying μ_0 affects the overall amplitude of the spinning dust component in units of $I_\nu/I_{H\alpha}$ while n_H does not (because of the density squared behavior of the spinning dust emission at these n_H), the value of D_0 changes as we move along the narrow valley of the χ^2 surface. It is important to note that small deviations from these parameters quickly lead to large χ^2 values. Further, given this set of environmental conditions and grain sizes, $D_0 = 1$ is ruled out, again implying either PAH depletion or modified grain size distributions in the WIM.

5.2. The Gum Nebula

In addition to our nearly full-sky template fit, we have also carried out smaller regional fits. Of particular interest are the four regions of the Gum Nebula shown in Figure 4 of DF08b. This is a region that is very bright in Hα but has little in the way of thermal dust emission or synchrotron. The null hypothesis is that the spectrum of this region should correspond almost entirely to a free–free spectrum.

Figure 9 shows the three-component model fit as well as the contour plots for the four regions of the Gum Nebula. The

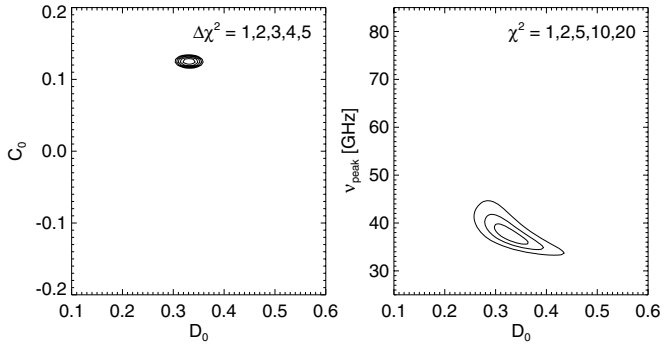

Figure 7. Left: $\Delta\chi^2$ contours in the (D_0, C_0) plane. The null hypothesis that the Hα-correlated emission follows a free–free power law with a contamination by the CMB spectrum is ruled out to very high significance ($\chi^2 \sim 710$ for 3 degrees of freedom at $D_0 = 0$). Right: χ^2 contours in the (D_0, ν_{peak}) plane. Though the peak frequency is not constrained to high accuracy, $\nu_{peak} \sim 37$ GHz is roughly the best-fit value.

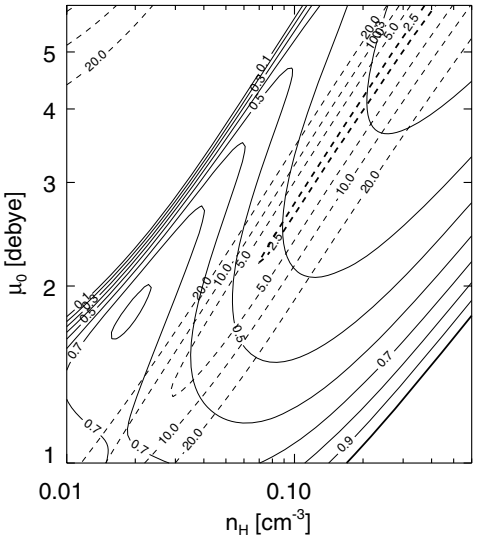

Figure 8. The χ^2 (dashed) and D_0 (solid) contours in the (n_H, μ_0) plane. There is a deep narrow valley in the χ^2 surface representing the near degeneracy in effects on the spinning dust peak frequency model with increasing n_H and decreasing μ_0. The values $n_H = 0.15\,\mathrm{cm}^{-3}$ and $\mu_0 = 3.5$ D produce an acceptable fit with $D_0 \approx 0.3$. Although D_0 does vary along the narrow valley in χ^2, $D_0 = 1$ does not yield an acceptable fit, indicating that either the PAHs are depleted in the WIM or the grain size distribution is altered.

[8] There is also the possibility as described in Wood & Reynolds (1999) and Mattila et al. (2007) that a significant fraction of the Hα intensity is generated in the form of *reflected* light. This would tend to overestimate the amount of Hα per free–free. However, in order to obtain a gas temperature of $T_{gas} \sim 8000$ K, the amount of reflected light would have to be >50% which seems unlikely (Wood & Reynolds (1999), estimate that at most 20% of the observed Hα at high latitudes is scattered light), especially in brighter regions like the Gum Nebula (see Figure 9) where three out of four of the regions have free–free emission consistent with temperatures $T_{gas} < 5000$ K. Another possibility is that our template fit of the spectrum is dominated by the strongest Hα features which naturally have a lower temperature.

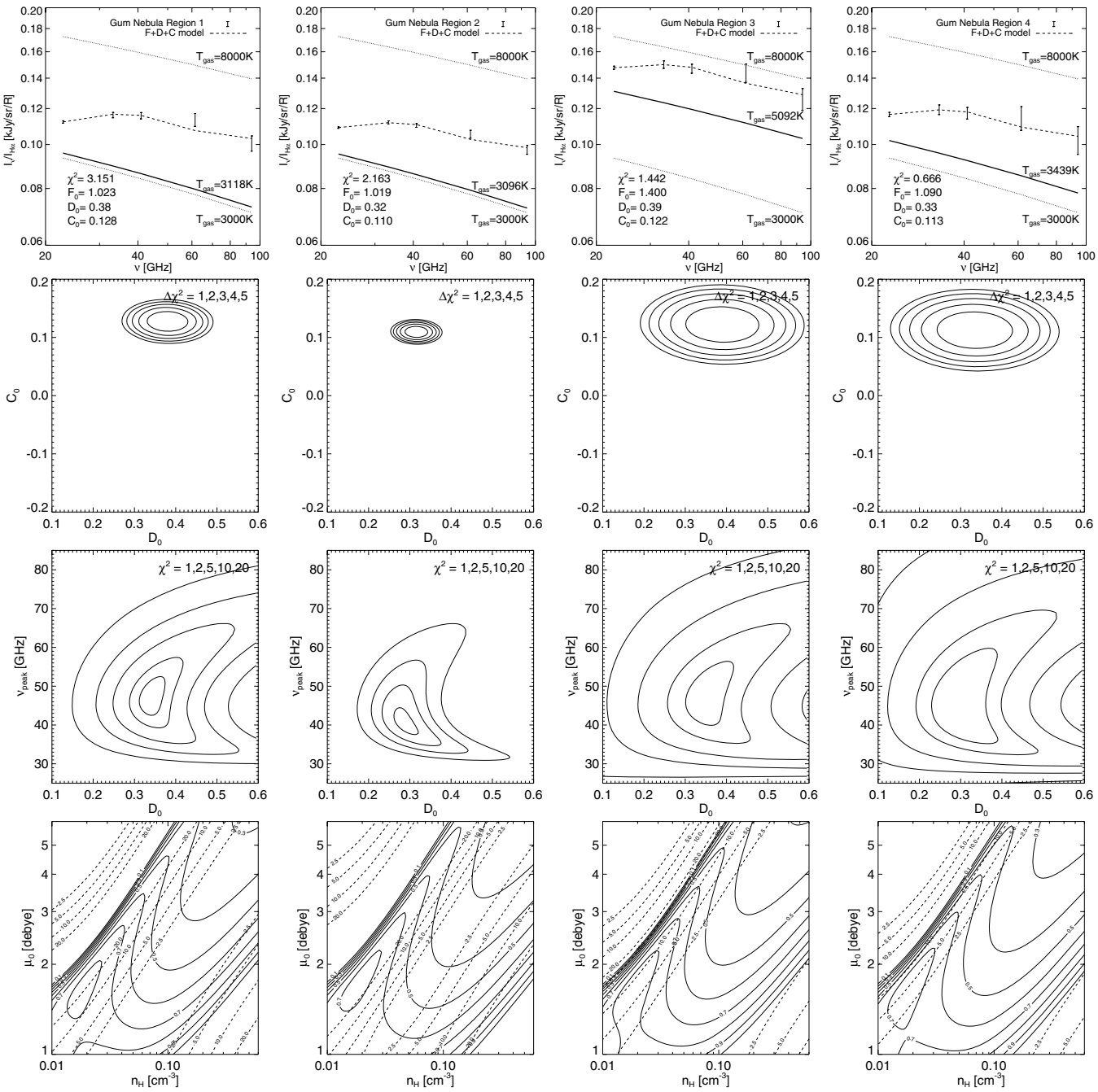

Figure 9. The same as Figures 6–8 except for the four regions of the Gum Nebula defined and illustrated in Dobler & Finkbeiner (2008b). In the top row, free–free per Hα spectra are shown for the best-fit $T_{\rm gas}$ (bold line) as well as $T_{\rm gas} = 3000$ K and 8000 K (dotted lines) for comparison. The null hypothesis that the Hα-correlated emission is well represented by a free–free spectrum with a CMB contamination is ruled out to high significance in all regions ($\chi^2 \gtrsim 13$ for 3 degrees of freedom at $D_0 = 0$).

bump in the Hα-correlated spectrum persists for all four regions, though the spinning dust amplitudes D_0 and CMB correlation bias amplitudes C_0 vary slightly from region to region. There is some evidence that the peak frequency $\nu_{\rm p}$ also varies slightly from region to region, but it is the least well constrained parameter and all four regions indicate roughly $\nu_{\rm p} \sim 35$–45 GHz. From the $\Delta\chi^2$ contours in the $(D_0,\ C_0)$ plane, we find that the null hypothesis of $D_0 = 0$ is ruled out at high confidence in all regions.

Due to the larger error bars in the template fit (the smaller regions include fewer pixels), the χ^2 valley in the $(n_{\rm H},\ \mu_0)$ plane is somewhat broader than in the full-sky fit. Nevertheless, all of the spectra are consistent with a WIM spinning dust spectrum with $n_{\rm H} \sim 0.1$ cm^{-3}, $\mu_0 \sim 2$ D, and $D_0 \sim 0.4$.

5.3. Thermal Dust-Correlated Emission

As shown in Figure 1, dust-correlated emission falls from 23 GHz to 60 GHz and it was this departure from a thermal spectrum which initially lead to speculation that this "anomalous" dust component originated from spinning grains. In this section, we fit our three-component model to these data but replace the WIM spinning dust model in Equation (5) with a CNM spinning dust model and the free–free component with a thermal dust spectrum $T = T_0 \times (\nu/94\ {\rm GHz})^{\beta_D}$. We choose

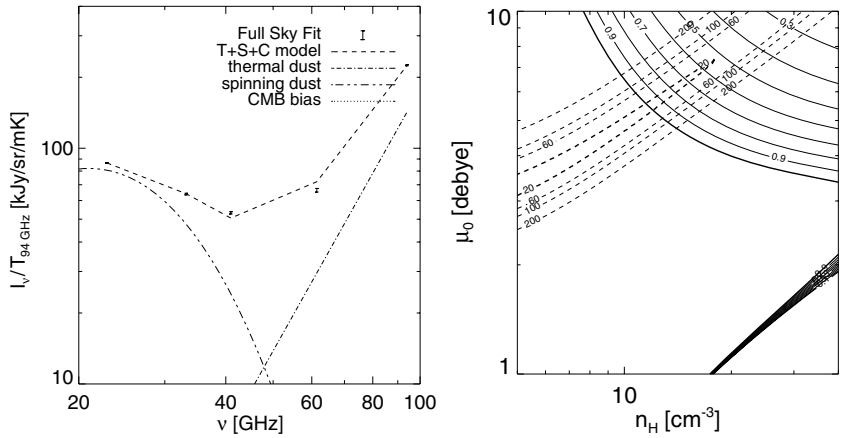

Figure 10. Left: a three-component model fit to the FDS99-correlated emission spectrum from 23 to 94 GHz. The fit includes a thermal dust component ($T \propto \nu^{1.7}$), a CNM spinning dust component ($n_{\rm H} = 11\,{\rm cm}^{-3}$ and $\mu_0 = 5.5$ D; see Table 2), and a CMB component. Close inspection reveals that the curvature in this single-component spinning dust spectrum is incompatible with the data and overpredicts the amplitude at 61 GHz. Right: the same as Figure 8 except for CNM parameters and fitting to FDS99-correlated emission. Although the amplitude is roughly $D_0 = 1$, the χ^2 values are unacceptably high. In fact, for the model in the left-hand panel, $\chi^2 = 45.3$. Thus, for reasonable CNM parameters, a single-component DL98 spinning dust model is ruled out at high confidence.

$\beta_D = 1.7$ but note that our results are not significantly changed for the range $1.5 < \beta_D < 2$.

The left-hand panel in Figure 10 shows the results of fitting a CNM spinning model to the *WMAP* dust-correlated spectrum. The spinning dust model has $n_{\rm H} = 11\ {\rm cm}^{-3}$ and $\mu_0 = 5.5$ D. From the figure, it is clear that this particular spinning dust spectrum is not a very good fit to the data ($\chi^2 = 45.3$), especially considering that there are few free parameters. However, the right-hand panel of Figure 10 indicates that, although the amplitude is approximately correct ($T_0 \approx 1.0$), for the CNM parameters there is no point in parameter space which yields a significantly better fit.

The poor fit is due to the fact that the 23, 33, and 41 GHz data points exhibit roughly power-law behavior ($T \propto \nu^{-2.83}$) so that the spinning dust spectrum has too much curvature to fit the data. This power-law behavior has lead several authors to misidentify this emission as "dust-correlated synchrotron;" however, both *WMAP* polarization data (Kogut et al. 2007) and data at lower frequencies over large areas (Finkbeiner et al. 2004; de Oliveira-Costa et al. 2004) argue strongly against the synchrotron hypothesis. Furthermore, we note that, along any line of sight, there may very well be regions with different environment and grain properties leading to a superposition of spinning dust spectra. For example, if we use a five-component model with three spinning dust spectra (plus thermal dust and CMB spectra) that have the parameters $(n_{\rm H}/{\rm cm}^{-3}, \mu_0/{\rm D}) = (5.0, 6.5)$, (11.0, 5.5), and (40.0, 4.7), then the FDS99-correlated spectrum is perfectly fitted by weighting these spinning dust components with weights 1.3, 0.1, and 0.15, respectively. This degeneracy between synchrotron and a superposition of spinning dust spectra can only be broken with sufficient frequency coverage. In particular full-sky, high-resolution maps between 5 and 15 GHz could eliminate the ambiguity.

Lastly, we point out that the anomalous dust-correlated emission in the CNM could originate from an emission mechanism that is neither synchrotron nor spinning dust. For example, Draine & Lazarian (1999) suggest that emission from magnetized dust grain could contribute to the total emission in the lower frequency *WMAP* bands. However, in the case of the WIM, the fact that the Hα map and the DL98 spinning dust models both scale roughly as density squared suggests that the bump in the *Hα-correlated* emission originates from spinning dust and *not* DL99 magnetic dust. Furthermore, the observations of Casassus et al. (2008) appear to strongly limit the contribution of magnetic grain materials to the microwave emission from dust.

6. ALTERNATIVE EXPLANATIONS FOR THE Hα-CORRELATED BUMP

In this section, we will address alternative explanations for the origin of the bump in the Hα-correlated emission. The alternatives listed here are not meant to be an exhaustive list of possibilities but rather constitute potentially important features of the maps, our fitting procedure, etc., and thus require careful attention about whether they can artificially generate a bump in our spectrum. For each of these, we argue why the bump is more likely to be explained by spinning dust.

6.1. Bandpass Effects

Although the spectra presented in previous sections consisted of five data points, the individual channels of *WMAP* have broad ($\Delta\nu/\nu \approx 0.2$) bandpasses that must be taken into account. For a given emission mechanism, the total intensity in a *WMAP* channel is the spectrum of that emission integrated over the bandpass of that channel,

$$I_b^{\rm tot} = \frac{\int I_\nu \omega(\nu) d\nu}{\int \omega(\nu) d\nu}, \tag{6}$$

where $I_b^{\rm tot}$ is the total intensity in band b and $\omega(\nu)$ is the bandpass for band b normalized so that $\int \omega(\nu) d\nu \equiv 1$. Thus, for a free–free spectrum ($I_\nu \propto \nu^{-0.15}$), the observed spectrum will be slightly modified from a straight power law when plotted against the CMB weighted band centers (see below). We find that the deviations are at the level of ∼1%. Nevertheless, this total intensity, evaluated at each band, is what must be used to fit the derived cross-correlation spectrum.

Additionally, the *WMAP* data themselves must be converted from thermodynamic ΔT to I_ν in each band assuming a CMB

weighted band center,[9]

$$\nu_{\rm CMB} = \frac{\int \nu I_\nu^{\rm CMB} \omega(\nu) d\nu}{\int I_\nu^{\rm CMB} \omega(\nu) d\nu}, \quad (7)$$

where the spectrum of the CMB $I_\nu^{\rm CMB} \propto \nu^2/{\rm plc}(\nu)$ (i.e., flat in thermodynamic ΔT). All of the fits presented in previous sections take the bandpass weighting into account, and we find that the changes to the results are also at the $\sim$1% level.

6.2. Dust Extinction and Masking Effects

It has long been known that, although a map of Hα is an excellent tracer of free–free emission from ionized gas, it is not perfect. In particular, extinction of Hα by dust makes the map a poor tracer of free–free in regions of high dust column density. To account for this Finkbeiner (2003, whose map we have used in this paper) applies a dust correction which assumes uniform mixing between the dust and gas. Dickinson et al. (2003) take a slightly different approach by matching slices through the Galactic plane to an extinction model plus dust column density model and attempting to directly measure the extinction.

The effects of dust on the Hα map could manifest themselves in two ways. First, recall that our mask is generated by avoiding regions where the extinction due to dust at Hα is $E(B-V) > 1$ mag. It is difficult to envision that our mask could have a sufficiently large impact on our derived spectrum to produce the bump, but it is instructive to consider the possibility. In Figure 11, we show the derived Hα-correlated spectrum for a wide range of dust cuts (i.e., for numerous masks). As can be seen in the figure, the bump feature is robust to variations in the mask.

The second potential issue is that perhaps the Hα map has been overcorrected for dust so that it is actually a rather poor tracer of free–free, potentially leading to the bump as a spurious artifact. To test this hypothesis, we performed our template fit with an Hα map that was not corrected for dust extinction at all. Even in this extreme case of *undercorrection*, we find that the bump persists. We conclude that the bump does not result from errors in the extinction correction of the Hα map.

6.3. CMB Cross-Correlation Bias

The CMB cross-correlation bias described above (and more extensively in DF08a) is both large and ubiquitous in CMB foreground analyses. Because the effect on the derived spectrum of each component can be substantial, it is important to rule out the possibility that this bias is producing the bump. This possibility represents the "null hypothesis" discussed in Section 5.1. The basic question is: can the derived cross-correlation spectrum be fitted by a simple linear combination of free–free and CMB spectra? As we showed in that section, this $D_0 = 0$ case is ruled out at *very* high confidence with a χ^2 per degree of freedom of 245 (for 3 degrees of freedom at $D_0 = 0$).

6.4. Cross-Correlation Between the Templates

If there is any chance spatial cross-correlation between the templates, then this will impact the shape of the derived spectra. Furthermore, if one of the templates is contaminated by Hα morphology or vice versa, then the spectrum of each foreground will be "contaminated" by the others. Again, a clear example of this would be poor dust correction of the Hα map adding dustlike morphology to that map. Another example would be reflection of Hα photons created in the plane off of dust at high latitudes, which would also imprint a dustlike morphology on the Hα map. There is also the fact that the WIM emits thermal radiation as well and so there is some Hα morphology present in the FDS99 map.

DF08b showed that the chance spatial cross-correlations between the templates used in the analysis is sufficiently small that there should be relatively little contamination of one foreground spectrum onto another. We explore this point in greater detail in the Appendix, where we specifically address the fact that WIM features appear at a low level in the dust map.

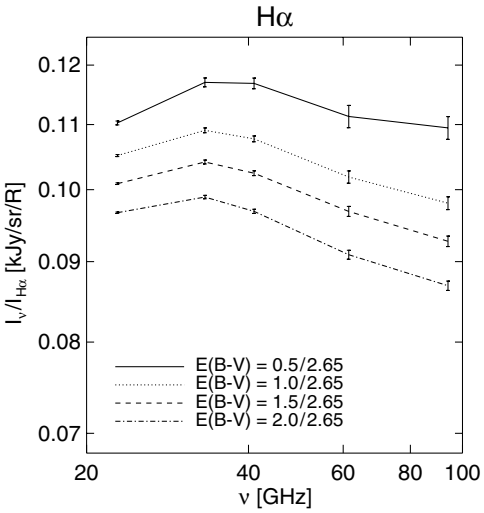

Figure 11. Foreground spectra derived via our multi-linear regression template fit as a function of the extinction cut used for the mask. The bump in the Hα-correlated emission persists for all mask definitions indicating that it is not due to improperly corrected extinction in the Hα map.

6.5. Variations of T_{gas} with Position

Gas temperatures in the interstellar medium are known to vary with position. For example, there is evidence that there is a decrease in $T_{\rm gas}$ toward the Galactic center (Quireza et al. 2006). However, even though relatively small variations in $T_{\rm gas}$ lead to large changes in the Hα to free–free ratio, the effect is simply an amplitude shift (Valls-Gabaud 1998). Thus, when we fit the nearly full sky, we are averaging over many regions with slightly different amplitudes, *but all with spectra* $\propto \nu^{-0.15}$. Thus, our resultant spectrum should be $\propto \nu^{-0.15}$ indicating that a superposition of many regions with varying $T_{\rm gas}$ would *not* produce a bump in the average spectrum.

6.6. Model-Independent Identification of the Anomalous Emission

Rather than attempting to address every possible contamination mechanism that could result in a bump in the Hα-correlated spectrum, it is possible to identify the bump *without the use of any template fitting and only using the WMAP data*. The top two panels of Figure 12 show the *WMAP* data at 23 GHz (with CMB5 subtracted) as well as the Hα map. We identify two regions that are bright in Hα and also bright at *K* band (23 GHz): ζ Oph near $(\ell,\ b) = (6,\ 23)$ deg and the Gum Nebula near $\ell = 260$ and $-22 < b < 17^\circ$. If the Hα map traces only

[9] By design the *WMAP* receivers measure energy and so the natural data unit is $\int I_\nu d\nu$; however, since they are then calibrated off of the CMB dipole, the data are presented in thermodynamic ΔT.

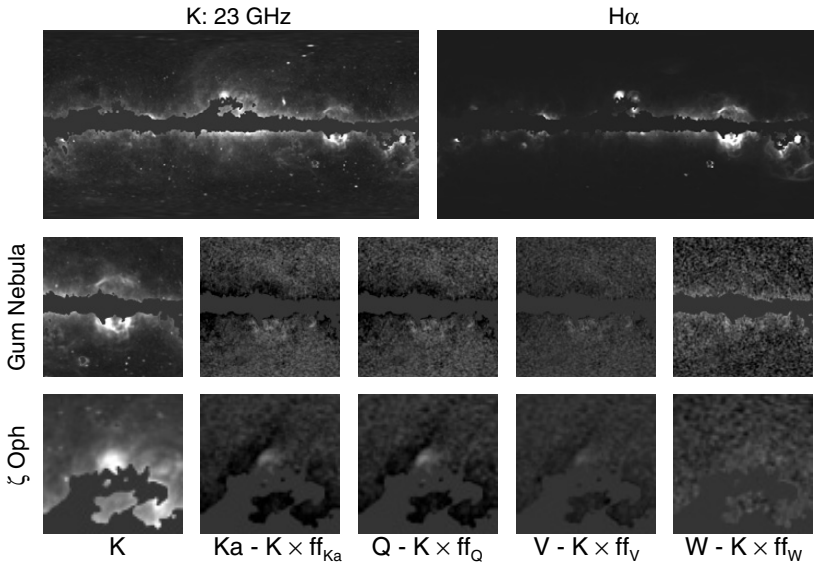

Figure 12. Top left: *WMAP K* band minus CMB5. Top right: the Hα map. First column: a cut out of *K* band around the Gum Nebula (row 1) and ζ Oph (row 2). Second through fifth columns: *K* band subtracted from Ka, *Q*, *V*, and *W* bands using a free–free $\nu^{-2.15}$ spectrum. Clearly, there is residual emission in both the southern Gum Nebula and the ζ Oph cloud using a free–free spectrum indicating the need for a separate component. This component is harder than free–free from 23 to 41 GHz and softer than free–free from 41 to 94 GHz, which is indicative of a spinning dust spectrum. Although there are significant regions of oversubtraction (due to the substantial synchrotron component at low frequencies), the Hα-correlated emission is clearly undersubtracted by a free–free spectrum.

free–free emission, then subtracting *K* band scaled by a free–free spectrum from Ka, *Q*, *V*, and *W* band should completely eliminate these features.

The bottom grid in Figure 12 shows *K* band in the left most column and then the result of subtracting *K* band scaled by a free–free spectrum from Ka, *Q*, *V*, and *W* bands (Columns 2, 3, 4, and 5, respectively) for both the Gum Nebula region (row 1) and the ζ Oph region (row 2). Since the spectrum of free–free is harder than synchrotron and softer than thermal dust, synchrotron emission is highly oversubtracted and thermal dust emission is undersubtracted (note the prominence of thermal dust emission in Column 5). What we find is that with a free–free spectrum, there is a clear excess in the southern Gum Nebula region and particularly in ζ Oph. The implication is that ζ Oph and the Gum Nebula contain an emission component which is *harder* than free–free from 23 GHz to 41 GHz, but softer than free–free from 41 GHz to 94 GHz. Furthermore, this spectrum is not soft enough at 23–61 GHz to be synchrotron, yet is vastly brighter than the expected thermal dust emission, so it cannot be any of the standard foreground components. Rather, it has a spinning dust type spectrum with peak frequency near $\sim$40 GHz.

7. DISCUSSION

We have repeated the multi-linear regression template fit outlined in DF08a on the five-year *WMAP* data and found that the anomalous "bump" at $\sim$40 GHz in the Hα-correlated emission spectrum persists and has in fact become more pronounced. The most significant changes in the spectrum from three-year to five-year data come from large-scale modes (particularly a large dipole at 61 GHz *V* band) of amplitude $\sim$10 μK that were corrected in the five-year data.

We interpret this bump as a WIM spinning dust component that is traced by the Hα map. We find that for WIM parameters the total spinning dust emission per grain scales roughly as the ambient ionized gas density squared (see Figure 5). Therefore, a map of emission measure (EM $= \int n_e^2 d\ell$) like the Hα map would be *expected* to trace this component.

Any derived foreground spectrum is subject to the CMB correlation bias (see DF08a) from chance spatial correlations of the foreground emission with the CMB. Thus, we fit a three-component model consisting of free–free, WIM spinning dust, and CMB spectra to the derived Hα-correlated emission in which the amplitude of each component is allowed to float. The best-fit model gives a value for the ion density of the ambient medium of $n_{\rm H} \sim 0.15$ cm^{-3} and a characteristic dipole moment for the grains of $\sim$3.5 D referenced to 1 nm grains. However, there is a strong degeneracy between these two parameters as they have similar effects on the peak frequency.

The amplitude of the spinning dust spectrum must be reduced by a factor $\sim$0.3 compared to the model to fit the data, possibly indicating that PAHs are depleted in the WIM. From the amplitude coefficient of the free–free component, we use the Hα to free–free ratio to infer a gas temperature of $\sim$3000 K. Near the peak frequency at 41 GHz, the total spinning dust emission is roughly 20% of the free–free emission. We also find that the bump persists in smaller regional fits of the Gum Nebula as well with roughly the same amplitude. There is some evidence that the peak frequency varies with region, but this parameter is the most poorly constrained in our analysis.

As in numerous other studies, we also find the now familiar rise in the *thermal dust*-correlated spectrum from 41 to 23 GHz from anomalous dust-correlated emission. An attempt to fit a three-component model of thermal dust, CNM spinning dust, and CMB spectra to the dust-correlated emission yields a poor fit. However, we expect that, along any line of sight, there will be multiple regions with different environmental properties so that the low-frequency dust-correlated emission may represent a superposition of spinning dust spectra. Although other possibilities exist for this emission (magnetic dust and "dust-correlated synchrotron" being two), we point out that since the Hα map is a density squared map, and since WIM spinning dust emission goes roughly as density squared, we believe it is very likely that the bump in the Hα-correlated emission represents a spinning dust component. *Magnetic dust emission would not correlate with Hα in this way.*

We have shown that the bump cannot be explained by numerous possible systematic uncertainties in our fit. For example, the bump cannot be the result of the CMB correlation bias because a fit to the spectrum with a two-component free–free plus CMB model yields a very bad $\chi^2 = 710$ with 3 degrees of freedom. It also cannot be due to poor correction for dust extinction of the Hα map since the bump persists even if the template fit is performed with a completely uncorrected map, nor is it sensitive to our choice of mask for which we cut on dust extinction of Hα. Variations in gas temperature with position and cross-correlation between the templates used in the fit are also incapable of producing the bump.

Perhaps the most striking visualization that the bump is not an artifact of the fitting procedure is by subtracting the *K* band *WMAP* data scaled with a free–free spectrum from Ka, *Q*, *V*, and *W* bands. This reveals that in regions that are very bright in *K* band and Hα which were thought to be completely free–free dominated at these frequencies (e.g., the Gum Nebula and ζ Oph), there is a positive residual at 33, 41, and 61 GHz. Scaling by a free–free plus bump spectrum instead removes the residual. The implication is that there is emission coming from these regions that has a spectrum that is harder than free–free from 23 to 41 GHz and then softer than free–free from 41 to 94 GHz, which resembles a spinning dust spectrum.

The interpretation of the dust-correlated anomalous emission as spinning dust (or magnetic dust) has been plagued by the fact that ancillary data sets at lower frequencies are needed to distinguish that emission from synchrotron. Here, we have shown that a turnover in the spinning dust spectrum is completely recoverable *within* the *WMAP* frequency range. The only surprise is that it correlates with the Hα map. In hindsight, this is not very surprising since the Hα map traces density squared emission, though it does suggest that there is no "true" template for the spinning dust. Rather, it is potentially ubiquitous and probably will not correlate precisely with any map of the sky. This will be especially important for future missions (e.g., *CMBPol*; see Dunkley et al. 2008; Fraisse et al. 2008) which will require very precise characterization of both the total intensity and polarization of spinning dust emission to measure cosmological parameters with increasing accuracy.

We acknowledge informative discussions with Simon Casassus, Clive Dickinson, Joanna Dunkley, Ben Gold, Gary Hinshaw, Al Kogut, and David Spergel. We thank Matt Haffner and Carl Heiles for insights on gas temperatures in the warm ionized medium, and Alex Lazarian, Chris Hirata, and Yacine Ali-Haïmoud for stimulating discussions on excitation mechanisms in spinning dust models. Some of the results in this paper were derived using HEALPix (Górski et al. 2005; Calabretta & Roukema 2007). This research made use of the IDL Astronomy User's Library at Goddard.[10] G.D. and D.P.F. are partially supported by NASA LTSA grant NAG5-12972. B.T.D. is partially supported by NSF grant AST-0406883.

APPENDIX

IMPERFECT TEMPLATE MORPHOLOGY

Here, we consider the effects of "contaminating" one of the templates with another, and determine the effects on the resultant spectra. We phrase this in terms of a template (denoted with primes) and a "true" map that perfectly traces the emission for the component we are solving for. We consider two cases. First, we consider that the Hα map is not a perfect tracer of free–free emission and show that this does not mix the spectrum of other foregrounds into the Hα-correlated spectrum. That is, the bump in the spectrum is not due to contamination effects from other foreground spectra. Second, we consider the case in which the dust template, FDS99, is tracing both a CNM and WIM spinning dust component at low frequencies. This case does have an impact on the spectrum, but we show that it cannot produce the observed bump and that it does not significantly impact our main conclusions.

A.1. Hα as an Imperfect Tracer of Free–Free

For the template fits the equation we are trying to solve, neglecting the CMB and the associated cross-correlation bias and considering only two foregrounds, is

$$a_1 H' + a_2 D = t_1 H + t_2 D, \tag{A1}$$

for a_1 and a_2, where H is the true Hα map which we assume exactly traces free–free emission, D is the dust map, t_1 and t_2 are the true amplitudes (at an arbitrary frequency), and H' is the observed Hα map (which may be contaminated in some way).

By multiplying Equation (A1) by H' and solving for a_1, we obtain

$$a_1 = t_1 \frac{\langle HH' \rangle}{\langle H'^2 \rangle} + t_2 \frac{\langle DH' \rangle}{\langle H'^2 \rangle} - a_2 \frac{\langle DH' \rangle}{\langle H'^2 \rangle} \tag{A2}$$

and likewise by multiplying by D and solving for a_2 we find

$$a_2 = t_2 + t_1 \frac{\langle DH \rangle}{\langle D^2 \rangle} - a_1 \frac{\langle DH' \rangle}{\langle D^2 \rangle}. \tag{A3}$$

To show that the Hα-correlated emission spectrum is not affected by the *spectrum* of the dust-correlated emission, we need to show that $a_1 \neq a_1(a_2, t_2)$. Plugging Equation (A3) into Equation (A2) we get

$$a_1 = t_1 \frac{\langle HH' \rangle}{\langle H'^2 \rangle} - t_1 \frac{\langle DH \rangle \langle DH' \rangle}{\langle D^2 \rangle \langle H'^2 \rangle} + a_1 \frac{\langle DH' \rangle \langle DH' \rangle}{\langle D^2 \rangle \langle H'^2 \rangle}, \tag{A4}$$

or

$$a_1 \left(1 - \frac{\langle DH' \rangle \langle DH' \rangle}{\langle D^2 \rangle \langle H'^2 \rangle} \right) = t_1 \left(\frac{\langle HH' \rangle}{\langle H'^2 \rangle} - \frac{\langle DH \rangle \langle DH' \rangle}{\langle D^2 \rangle \langle H'^2 \rangle} \right). \tag{A5}$$

Equation (A5) shows two things. First, a_1 does not depend on either a_2 or t_2, implying that the spectrum of Hα-correlated emission does not depend on either the spectrum or the inferred spectrum of dust-correlated emission. But there is an overall multiplicative normalization that depends on cross-correlations of H, H', and D. Note that as $H \rightarrow H'$, $a_1 \rightarrow t_1$. Equation (A5) is the general case; but now suppose we assume a specific form for H', namely, we mix in a bit of the dust map so that $H' = H + \epsilon D$. This can originate from imperfect dust correction of the Hα map or scattering of Hα photons off of dust, for example. Then, the right-hand side of Equation (A5) reads

$$\begin{aligned} & t_1 \left(\frac{\langle HH' \rangle}{\langle H'^2 \rangle} - \frac{\langle DH \rangle \langle DH' \rangle}{\langle D^2 \rangle \langle H'^2 \rangle} \right) \\ & = t_1 \left(\frac{\langle (H' - \epsilon D) H' \rangle}{\langle H'^2 \rangle} - \frac{\langle D(H' - \epsilon D) \rangle \langle DH' \rangle}{\langle D^2 \rangle \langle H'^2 \rangle} \right) \\ & = t_1 \left(1 - \epsilon \frac{\langle DH' \rangle}{\langle H'^2 \rangle} - \frac{\langle DH' \rangle \langle DH' \rangle}{\langle D^2 \rangle \langle H'^2 \rangle} + \epsilon \frac{\langle D^2 \rangle \langle DH' \rangle}{\langle D^2 \rangle \langle H'^2 \rangle} \right) \\ & = t_1 \left(1 - \frac{\langle DH' \rangle \langle DH' \rangle}{\langle D^2 \rangle \langle H'^2 \rangle} \right). \end{aligned} \tag{A6}$$

[10] Available at http://idlastro.gsfc.nasa.gov.

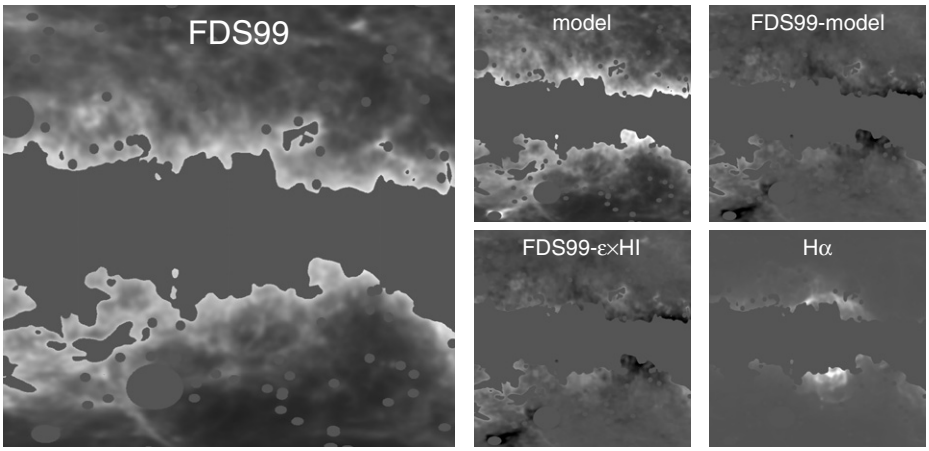

Figure 13. An illustration of the contamination of FDS99 by Hα morphology. The left panel shows the FDS99 dust map centered on the Gum Nebula ($\{\ell,\ b\} = \{260,\ 0\}$, a strong Hα feature). The top middle panel shows the best-fit FDS99 $= \epsilon_0 L + \delta_0 H$, where L is a map of H I emission and H is the Hα map. The top right panel shows that the difference between the model and the FDS99 map contains very little Hα morphology (lower right panel). Nevertheless, the effect is subtle as shown in the residual plus $\delta_0 H$ map in the lower middle panel. Our fit of the level of contamination of the FDS99 map by Hα morphology is $\delta_0 \sim 4.5 \times 10^{-5}$ mK R^{-1}.

Comparing the term in parentheses with the left-hand side of Equation (A5) shows, that, in the case where H' is a linear superposition of H and D, $a_1 = t_1$. That is, we recover the true spectrum. The bottom line is that, if the Hα map does not exactly trace the free–free morphology, the spectrum will be affected, but only at most by a constant multiplicative factor (i.e., it will not produce a bump in the spectrum).

A.2. FDS99 as a Tracer of Both WIM and CNM Spinning Dust

So far we have assumed that FDS99 is a tracer of exclusively the CNM dust, as if WIM dust only appeared as Hα-correlated emission. While the WIM dust indeed has a hotter color temperature (e.g., in the 60/100 μm ratio) than CNM dust, it certainly also appears in the FDS99 map. Therefore, in our regression analysis, fitting the CNM component with the FDS99 template will inadvertently absorb some of the WIM emission and affect the inferred spectrum of the WIM. The sense of the effect is to bias the Hα-correlated WIM emission with some amount of the CNM spectrum, pushing the WIM spectrum to higher peak frequency and lower amplitude. In this section, we estimate the extent of this bias.

In order to calculate an estimate of the contamination of FDS99 by Hα morphology, we model the FDS99 map as a linear combination of maps of H I emission and Hα emission,

$$D = \epsilon_0 L + \delta_0 H, \tag{A7}$$

where, again, H is the Hα map, and L is the Kalberla et al. (2005) H I map. With this notation, δ_0 has the units of mK R^{-1}. We solve the above equation over unmasked pixels (where the mask consists of the point-source mask described in Section 2.1 plus a masking of all pixels for which the dust extinction at Hα is $2.65E(B-V) > 0.5$ mag) and find that $\delta_0 \sim 4.5 \times 10^{-5}$ mK R^{-1}. Although this value varies slightly from region to region (Heiles et al. 1999), the contamination is very small and extremely subtle (see Figure 13). Nevertheless, based on our value of δ_0, Hα morphology does indeed "contaminate" the FDS99 map since the large grains in the WIM emit thermal radiation at 94 GHz as well.

To calculate the effect on the inferred spectrum, we can use the same procedure as Section A.1 but now taking $D' \rightarrow D + \delta_0 H$. It is straightforward to show that the recovered Hα-correlated spectrum becomes

$$a_1 = t_1 - \delta_0 t_2. \tag{A8}$$

That is, the inferred Hα-correlated spectrum is contaminated by the FDS99-correlated spectrum at a level that is given by δ_0. Assuming that H exactly traces both the free–free emission and the WIM spinning dust emission and that D exactly traces CNM emission (thermal and spinning dust), the implication is that the bump in the inferred spectrum of the Hα-correlated emission represents the WIM spinning dust spectrum *minus* some amount of the CNM spinning dust spectrum, determined by how much the Hα morphology has leaked into the FDS99 map via large grain thermal emission in the WIM.

The left panel of Figure 14 shows the level of contamination of the Hα-correlated spectra by taking $D' =$ FDS99 $- \delta \times$ Hα as a tracer of CNM dust. As expected from Equation (A8), for large values of δ, the Hα map is being oversubtracted from FDS99 and the resultant spectrum is highly contaminated by a CNM thermal plus spinning dust spectrum (compare Figures 6 and 10). For $\delta = 0$ mK R^{-1}, on the other hand, some of the WIM spinning dust bump is being absorbed in the D'-correlated spectrum and so the bump in the Hα-correlated spectrum represents a WIM spinning dust minus some CNM spinning dust spectrum. Based on the fit in Equation (A7), the $\delta = \delta_0 \approx 4 \times 10^{-5}$ mK R^{-1} case is a nearly pure mixture of free–free plus CMB plus WIM spinning dust spectrum.

However, since the WIM does also emit thermal dust radiation, if we assume that FDS99 is a perfect representation of the thermal emission at 94 GHz, then removing the WIM (Hα) morphology from FDS99 implies that the Hα-correlated spectrum also contains that thermal emission. We can estimate the amplitude of this effect by assuming that the WIM thermal emission has a ν^β dependence on frequency with $\beta = 3.7$ (in intensity units, $\beta = 1.7$ in antenna temperature) and adding $\delta \times H \times (\nu/94\ \mathrm{GHz})^{3.7}$ back into the Hα-correlated spectrum. This is equivalent to setting,

$$D' = \mathrm{FDS99} - \left[1 - \left(\frac{\nu}{94\ \mathrm{GHz}}\right)^{1.7}\right] \times \delta \times \mathrm{H}\alpha. \tag{A9}$$

The resultant spectra are shown in the middle panel of Figure 14. In this case, the bump is ideally due to *only* spinning dust emission from the WIM for $\delta = 4 \times 10^{-5}$ mK R^{-1}. For larger

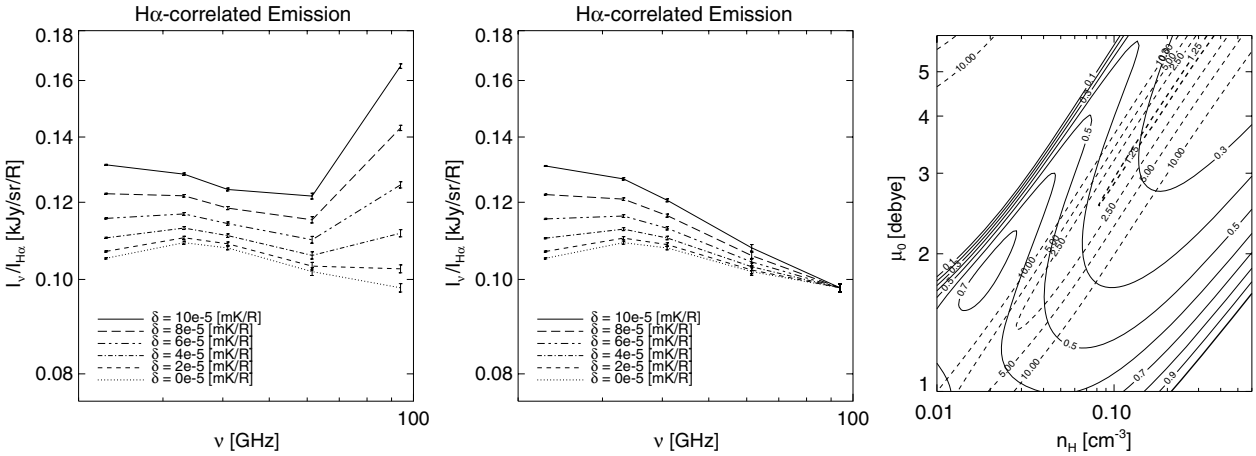

Figure 14. Left: the spectrum of Hα-correlated emission using FDS99 $-\ \delta \times$ Hα as a CNM template for various values of δ. Note that $\delta \sim 4 \times 10^{-5}$ mK R^{-1} is roughly required to appropriately remove Hα morphology from FDS99 as shown in Figure 13. As expected, as δ is increased, the spectrum from Figure 6 is contaminated with the FDS99-correlated spectrum in Figure 10 (see the text, Equation (A8)). Middle: the spectrum of Hα-correlated emission assuming that FDS99 exactly traces thermal dust emission with $T_{\rm dust} = {\rm FDS99} \times (\nu/94\ {\rm GHz})^{1.7}$. For $\delta = 0$ mK R^{-1}, the bump in the Hα-correlated spectrum represents the difference of WIM and CNM spectra, for $\delta = 4 \times 10^{-5}$ mK R^{-1}, the spectrum is almost entirely WIM, and as δ is increased further, the bump represents an addition of WIM plus increasingly more CNM spectra. Indeed, the peak frequency moves to the lower CNM value as δ gets large. Right: the χ^2 (dashed) and D_0 contours in the ($n_{\rm H}$, μ_0) plane for the spectrum shown in the middle panel with $\delta = 4 \times 10^{-5}$ mK R^{-1}. With this small level of contamination, our results for the best-fit $n_{\rm H}$, μ_0, and D_0 values are almost completely unchanged (compare Figure 8).

values of δ, the CNM spinning dust spectrum begins to leak into the fit so that by $\delta = 10 \times 10^{-5}$ mK R^{-1}, the spinning dust bump has moved toward the lower CNM value, and the amplitude has increased since the WIM and CNM spectra are now both present in the data.

Lastly, the right panel of Figure 14 shows χ^2 and D_0 contours in the ($n_{\rm H}$, μ_0) plane for a free–free plus CMB plus WIM spinning dust fit to the $\delta = 4 \times 10^{-5}$ mK R^{-1} spectra in the middle panel of Figure 14. These contours indicate that the best-fit values of $n_{\rm H}$ and μ_0 are not significantly affected by the presence of WIM morphology in the FDS99 map for our estimate of $\delta = 4 \times 10^{-5}$ mK R^{-1}. Nevertheless, the exact level of PAH depletion measured by our technique (D_0) will depend on precisely how one estimates the WIM leakage in FDS99. We defer a detailed analysis of this to future work.

REFERENCES

Ali-Haïmoud, Y., Hirata, C. M., & Dickinson, C. 2009, MNRAS, 395, 1065
Bennett, C. L., et al. 2003, ApJS, 148, 97
Boughn, S. P., & Pober, J. C. 2007, ApJ, 661, 938
Calabretta, M. R., & Roukema, B. F. 2007, MNRAS, 381, 865
Casassus, S., et al. 2008, MNRAS, 391, 1075
COBE Diffuse Infrared Background Experiment (DIRBE) Explanatory Supplement 1995, *COBE* Ref. Pub. No. 95-A, ed. M. G. Hauser, T. Kelsall, D. Leisawitz, & Weiland, J. 1995 (Greenbelt, MD: NASA/GSFC), available electronically from the NSSDC [*COBE* DIRBE Exp. Supp.]
COBE Far Infrared Absolute Spectrophotometer (FIRAS) Explanatory Supplement 1997, *COBE* Ref. Pub. No. 97-C, ed. S. Brodd, D. J. Fixsen, K. A. Jensen, J. C. Mather, & R. A. Shafer (Greenbelt, MD: NASA/GSFC), Version 4, available in electronic form from the NSSDC [*COBE* FIRAS Exp. Supp.]
Davies, R. D., et al. 2006, MNRAS, 370, 1125
de Oliveira-Costa, A., et al. 2004, ApJ, 606, L89
Dennison, B., Simonetti, J. H., & Topasna, G. 1998, PASA, 15, 147
Dickinson, C., Davies, R. D., & Davis, R. J. 2003, MNRAS, 341, 369
Dobler, G., & Finkbeiner, D. P. 2008a, ApJ, 680, 1222
Dobler, G., & Finkbeiner, D. P. 2008b, ApJ, 680, 1235
Draine, B. T., & Lazarian, A. 1998a, ApJ, 494, L19
Draine, B. T., & Lazarian, A. 1998b, ApJ, 508, 157
Draine, B. T., & Lazarian, A. 1999, ApJ, 512, 740
Draine, B. T., & Li, A. 2007, ApJ, 657, 810
Dunkley, J., et al. 2008, arXiv:0811.3915
Finkbeiner, D. P. 2003, ApJS, 146, 407
Finkbeiner, D. P. 2004, ApJ, 614, 186
Finkbeiner, D. P., Davis, M., & Schlegel, D. J. 1999, ApJ, 524, 867
Finkbeiner, D. P., Langston, G. I., & Minter, A. H. 2004, ApJ, 617, 350
Fraisse, A. A., et al. 2008, arXiv:0811.3920
Gaustad, J. E., McCullough, P. R., Rosing, W., & Van Buren, D. 2001, PASP, 113, 1326
Górski, K. M., Hivon, E., Banday, A. J., Wandelt, B. D., Hansen, F. K., Reinecke, M., & Bartelmann, M. 2005, ApJ, 622, 759
Haslam, C. G. T., Stoffel, H., Salter, C. J., & Wilson, W. E. 1982, A&AS, 47, 1
Haffner, L. M., Reynolds, R. J., Tufte, S. L., Madsen, G. J., Jaehnig, K. P., & Percival, J. W. 2003, ApJS, 149, 405
Heiles, C. 2001, ApJ, 551, L105
Heiles, C., Haffner, L. M., & Reynolds, R. J. 1999, ASPC, 168, 211
Hinshaw, G., et al. 2007, ApJS, 170, 288
Hinshaw, G., et al. 2009, ApJS, 180, 225
Kalberla, P. M. W., et al. 2005, A&A, 440, 775
Kogut, A., et al. 2007, ApJ, 665, 355
La Porta, L., Burigana, C., Reich, W., & Reich, P. 2008, A&A, 479, 641
Madsen, G. J., Reynolds, R. J., & Haffner, L. M. 2006, ApJ, 652, 401
Mattila, K., Juvela, M., & Lehtinen, K. 2007, ApJ, 654, L131
Page, L., et al. 2007, ApJS, 170, 335
Quireza, C., et al. 2006, ApJ, 653, 1226
Schlegel, D. J., Finkbeiner, D. P., & Davis, M. 1998, ApJ, 500, 525
Valls-Gabaud, D. 1998, PASA, 15, 111
Wheelock, S. L., et al. 1994, *IRAS* Sky Survey Atlas: Explanatory Supplement, JPL Publication 94-11 (Pasadena, CA: JPL)
Wood, K., & Reynolds, R. J. 1999, ApJ, 525, 799